ELSEVIER

Journal of Electron Spectroscopy and Related Phenomena 126 (2002) 145–162

JOURNAL OF ELECTRON SPECTROSCOPY and Related Phenomena

www.elsevier.com/locate/elspec

High resolution angle-resolved photoemission study of high temperature superconductors: charge-ordering, bilayer splitting and electron–phonon coupling

X.J. Zhou[a,b,*], Z. Hussain[b], Z.-X. Shen[a]

[a]*Department of Physics, Applied Physics and Stanford Synchrotron Radiation Laboratory, Stanford University, Stanford, CA 94305, USA*

[b]*Advanced Light Source, Lawrence Berkeley National Lab., Berkeley, CA 94720, USA*

Abstract

The latest development of angle-resolved photoemission spectroscopy (ARPES) technique has seen extremely high energy resolution and momentum resolution, as well as multiple angle detection. These advancements have led to new findings through efficient Fermi surface mapping, fine electronic structure resolving, and direct determination of electron self-energy. In this paper, we will highlight some recent high resolution ARPES work on high temperature superconductors. These include: (1) charge-ordering and evolution of electronic structure with doping; (2) bilayer splitting and Fermi surface topology of Bi2212; and (3) strong electron–phonon coupling and electron–electron interaction in high temperature superconductors.

Keywords: Angle-resolved photoemission spectroscopy (ARPES); Superconductors; Bi2212

1. Introduction

Despite extensive effort since the discovery of high temperature cuprate superconductors in 1986 [1], the mechanism of high temperature superconductivity remains a major challenge in physics [2]. All cuprate superconductors contain CuO_2 planes in their crystal structure which is believed to be responsible for superconductivity; the CuO_2 planes are sandwiched between various block layers which also serve as charge reservoirs to dope CuO_2 planes [3,4]. Without doping, the parent compound is an antiferromagnetic insulator; superconductivity occurs only in an appropriate doping range (Fig. 1) [5]. The doping level at which a maximum critical temperature (T_c) is achieved is usually denoted as optimal doping; the whole superconducting region is then divided into the underdoped region with less charge carriers and the overdoped region with more charge carriers. Besides the record high T_c, high temperature superconductors are found to exhibit many unusual physical properties, both in the normal state and in the superconducting state [5]. In the superconducting state, although it has long been realized that superconductivity still involves Cooper pairs [6], as in the traditional BCS theory [7,8], the experimentally determined *d*-wave pairing [9] differs from the usual *s*-wave pairing mediated by phonons [10,11]. The identification of the pairing mechanism in cuprate

*Corresponding author.
E-mail address: xjzhou@lbl.gov (X.J. Zhou).

0368-2048/02/$ – see front matter
PII: S0368-2048(02)00149-4

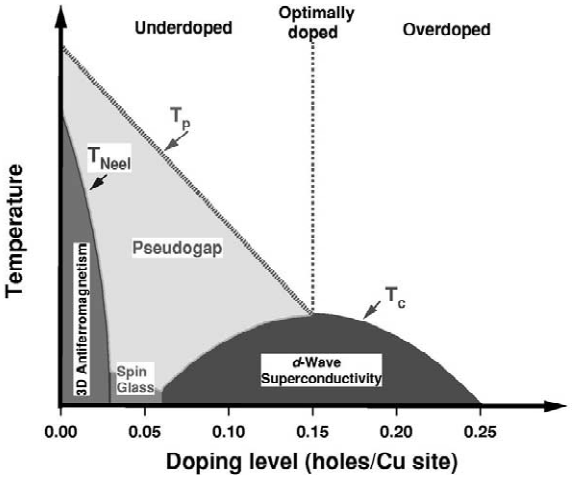

Fig. 1. Electronic phase diagram of high temperature superconductors.

superconductors remains an outstanding issue [12]. The normal state properties, particularly in the underdoped region, have been found to be at odds with conventional metals which are usually described by Fermi liquid theory; instead, they fit better with the marginal Fermi liquid phenomenology [13]. Most notable is the observation of the pseudogap state in the underdoped region above T_c [14]. In light of all these anomalies, it has been a matter of debate whether a new paradigm is needed to understand high temperature superconductivity [2].

Angle-resolved photoemission spectroscopy (ARPES) is a standard technique for studying the electronic structure of materials [15]; it has proven to be particularly powerful for investigating high temperature superconductors and other strongly correlated electron systems [16,17]. When light is incident on a sample, it kicks out electrons. The electronic structure of the material under study can be inferred from measuring the intensity of the photoemitted electrons as a function of their kinetic energy and their emission angle [15]. Under sudden approximation, angle-resolved photoemission measures single-particle spectral function $A(k, \omega)$, weighted by matrix element M and Fermi function $f(\omega)$: $I \sim A(k, \omega)|M|^2 f(\omega)$ [18,19]. The hole spectral function can be written in terms of self-energy $\Sigma(\omega, k) = \mathrm{Re}\Sigma(\omega, k) + i\mathrm{Im}\Sigma(\omega, k)$ as:

$$A(k, \omega) = \frac{1}{\pi} \frac{|\mathrm{Im}\Sigma(\omega, k)|}{[\hbar\omega - \epsilon_k - \mathrm{Re}\Sigma(\omega, k)]^2 + \mathrm{Im}\Sigma(\omega, k)^2} \quad (1)$$

where ϵ_k represents the band dispersion without interaction, $\mathrm{Re}\Sigma(k, \omega)$ and $\mathrm{Im}\Sigma(k, \omega)$ represent the real part and imaginary part of electron self-energy, respectively. Many important information about the electronic structure of materials can be obtained from $A(k, \omega)$, such as the determination of Fermi surface and the investigation of electron dynamics in terms of self-energy measurement.

ARPES has provided key experimental insights in revealing the electronic structure of high temperature superconductors [16]. These include, among others, the earliest identification of dispersion and large Fermi surface [20], an anisotropic superconducting gap suggestive of *d*-wave order parameter [21], and an observation of pseudogap in the underdoped samples [22]. With the latest advancement of electron energy analyzer for ARPES, new findings are made possible by taking advantage of its extremely high momentum resolution (up to ± 0.05 degree) as well as its high energy resolution (up to ~1 meV). This can be exemplified by the observation of an anisotropic superconducting gap in the electron-doped $(Nd,Ce)_2CuO_4$ superconductor ($T_c = 25$ K) where a maximum gap is ~2 meV [23], and the measurement of superconducting gap on the order of ~1 meV even in conventional metal superconductors, such as Pb and Nb [24]. The refined momentum resolution enables the investigation of Fermi surface with unprecedented details [25]. As a result, it is now possible to reveal fine details in the electronic structure and investigate the electron dynamics by directly measuring electron self-energy, as we will illustrate below.

In realizing the critical importance of high energy resolution and high momentum resolution for angle-resolved photoemission, a new beamline and an ARPES endstation (project name: High Energy Resolution Spectroscopy, HERS) were proposed in 1996 with strong support from Neville Smith as the scientific director of ALS, and started commissioning by the end of 1998. Equipped with an undulator and SGM monochromators, the photon energy of the beamline can vary between 20 and 340 eV with a

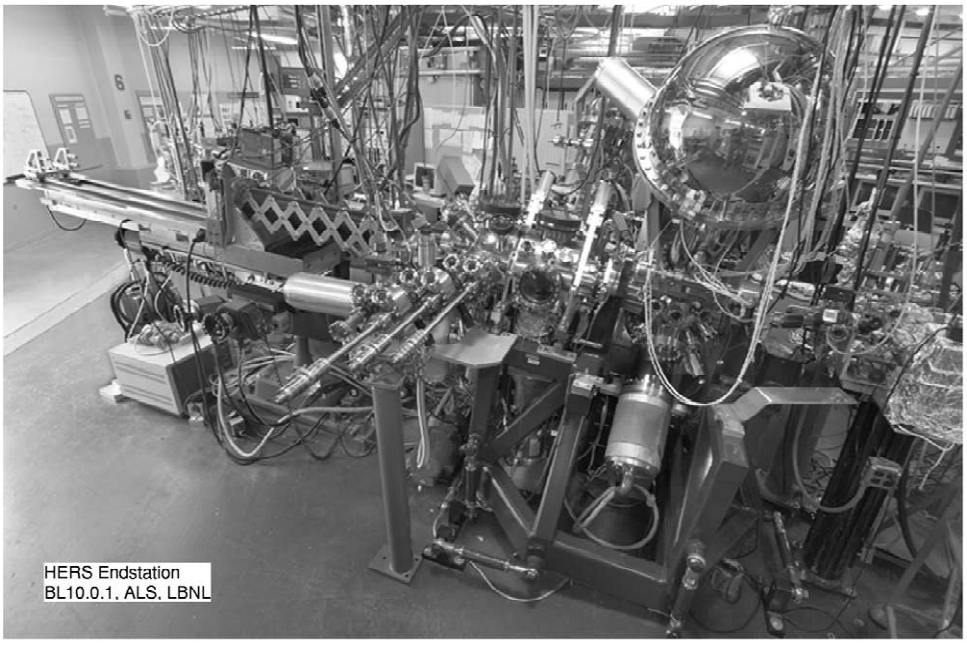

Fig. 2. Angle-resolved photoemission setup on Beamline 10.0.1 at ALS, Lawrence Berkeley National Lab.

resolving power of 10,000. The HERS endstation (Fig. 2) consists of three chambers: the Prep Chamber for sample preparation; the Characterization Chamber for doing low energy electron diffraction (LEED) on sample surface; and the Measurement Chamber for angle resolved photoemission. The design and commissioning of this station benefited from the experience of Chuck Fadley's group on Beamline 9.3.2. A new chamber was recently added on top of the Characterization Chamber for cleaning metal surfaces and making thin films. The heart of the HERS setup is the Scienta analyzer which, for SES200 model, can reach an energy resolution of ~5 meV and angle resolution of ± 0.15 degree, with 14 degrees of simultaneous angle coverage. Recently the analyzer has been replaced with the latest SES2002 model which reaches an energy resolution of 1.8 meV. The new analyzer has two angular modes: one has similar angle coverage (14 degrees) and angular resolution (± 0.15 degree) as SES200 and the second mode has ~8 degrees coverage and an angular resolution of ± 0.05 degree. The sample is mounted on a manipulator which has three degrees of translational freedom and two degrees of rotational freedom; the sample temperature can be varied from 15 K to 450 K with helium cooling and a heater. The Scienta analyzer, together with the Measurement Chamber, is rotatable with respect to the beam, thus facilitating the investigation of polarization dependence.

The HERS endstation is aimed at studying strongly correlated electron systems, particularly high temperature superconductors. Various materials have been measured using the system, including colossal magnetoresistance (CMR) materials [26], heavy Fermion materials [27], C_{60} and low dimensional systems, to name a few. In this paper, we briefly review recent ARPES work on high temperature superconductors using this system [28–39]. Instead of detailing various results, we focus on three examples of our studies.

2. Charge ordering and evolution of electronic structure with doping

The undoped parent compound of high temperature superconductors is a Mott insulator due to strong on-site electron–electron interaction. With the introduction of charge carriers into the CuO_2 planes, it

evolves into superconductors at an appropriate doping range (Fig. 1). In order to understand such a dramatic transition of physical properties, it is essential to investigate how the electronic structure evolves with doping. A related issue is the distribution of charge carriers in the CuO_2 planes, as there exist theoretical reasons that the charge may separate at nanoscale [40]. Because of the strong electron correlation, it was long realized that the holes tend to phase separate into hole-rich and hole-poor regions. One particular form of phase separation is stripes where the charge carriers segregate into one-dimensional domain walls (charge stripes) [40–65]. Static stripe formation in cuprates was first identified in $(La_{2-x-y}Nd_ySr_x)CuO_4$ (Nd-LSCO) system from neutron scattering [66], with further evidences from other techniques [67–69]. Similar signatures identified in $(La_{2-x}Sr_x)CuO_4$ (LSCO) [70,68] and other high temperature superconductors [71] point to the possible existence of stripes in these systems, albeit of dynamic nature. A key issue about this new electronic state of matter concerns whether the stripe phase is intrinsically metallic or insulating, given its spin and charge ordered nature, and

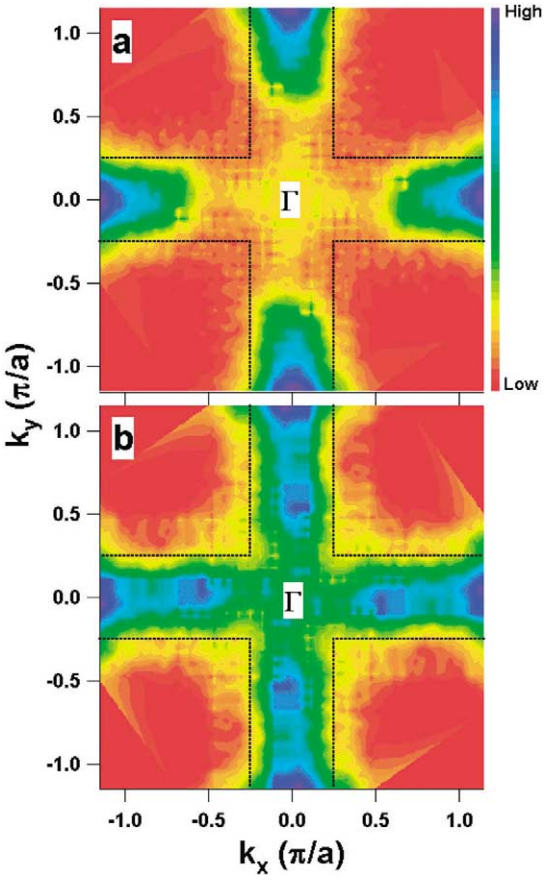

Fig. 3. Spectral weight distribution of $(La_{1.28}Nd_{0.6}Sr_{0.12})CuO_4$. In this measurement geometry, the electrical field of the incident light is nearly perpendicular to the sample surface. (a) shows low energy spectral weight integrated within 100 meV of the Fermi level while (b) shows the spectral weight integrated within 500 meV of the Fermi level. The dashed black lines in (a) and (b) define the regions where the spectral weight is mainly concentrated.

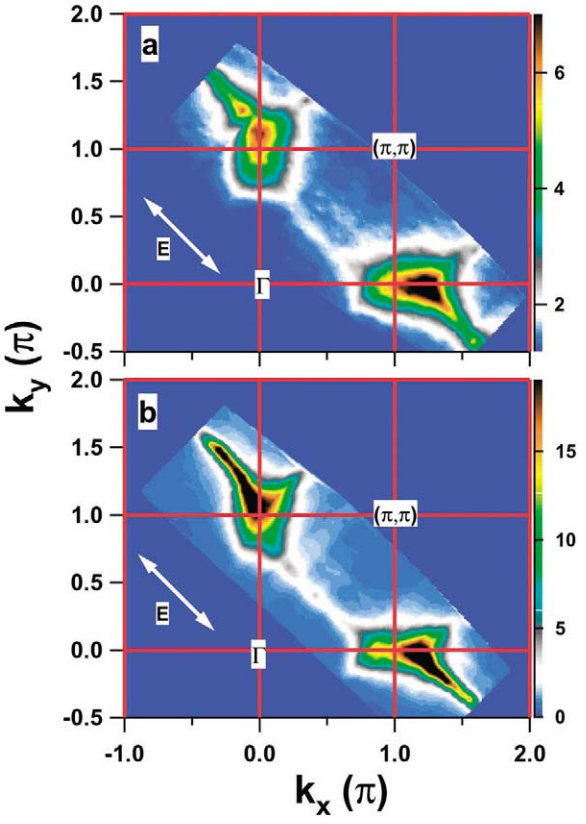

Fig. 4. Spectral weight distribution of $(La_{1.25}Nd_{0.6}Sr_{0.15})CuO_4$ (a) and $(La_{1.85}Sr_{0.15})CuO_4$ (b) integrated within 30 meV energy window near the Fermi level. In this measurement geometry, the electrical field of the incident light is nearly parallel to the sample surface, as indicated as white arrows in (a) and (b).

whether it is a natural route to realize high temperature superconductivity [42,51]. Understanding the electronic structure of the stripe phase is a prerequisite for addressing these issues.

We have carried out extensive ARPES measurements on $(La_{2-x-y}Nd_ySr_x)CuO_4$ and $(La_{2-x}Sr_x)CuO_4$ ($x=0\sim0.30$) systems [28,31,34,37,38]. The Nd-LSCO is a model system with static stripes while LSCO shows possible dynamic stripes over a certain doping range ($0.05<x<0.25$). Fig. 3 shows the spectral weight distribution of Nd-LSCO, measured under a geometry such that the electrical field vector $\vec{E}$ of the incident light is nearly normal to the sample surface [28]. The low energy spectral weight (Fig. 3(a)) is found to be mainly confined near the $(\pi, 0)$ and $(0, \pi)$ antinodal regions. Upon increasing the energy integration window, the spectral weight extends towards the center of the Brillouin zone (Γ point) (Fig. 3(b)). In both cases, the spectral weight is confined within straight boundaries from which a one-dimensional (1D) Fermi surface can be inferred. This observation, together with the suppression of the spectral weight along the $(0, 0)$–(π, π) nodal direction, seems to be consistent with the rigid stripe model calculation and was interpreted this way [60,62,63]. However, when we measured the samples under another geometry where the electrical field vector $\vec{E}$ of the incident light is parallel to the sample surface, in addition to the similar straight segments near $(0, \pi)$ and $(\pi, 0)$ as seen in Fig. 3(a), we have observed nodal spectral weight with an associated Fermi surface (Fig. 4) [31,34]. Apparently the matrix element effect is involved in these measurements [34]. More importantly, it indicates that the electronic structure of the charge-ordered state is more complicated than a rigid 1D system.

Fig. 5 shows the near Fermi level (E_F) spectral weight distribution of LSCO which covers the whole doping range ($x=0.0\sim0.30$). This serves to illustrate how the electronic structure evolves with doping and sheds light on that of charge-ordered system. For the undoped $x\sim0$ sample (there is a minuscule amount of residual extra oxygen in the La_2CuO_4 sample we measured), the lower Hubbard band (LHB) is located at a binding energy of ~0.5 eV (Fig. 6). Upon doping, new electronic states are created within the insulating gap while the LHB remains pinned at the same energy. This is the so-called two-component electronic structure [72] that can be attributed to the hole-poor and hole-rich regions in a nanoscale phase-separated system such as the stripe phase. The new nodal state from the hole-rich region is close to the Fermi level while the antinodal state exhibits a pseudogap in the underdoped region; this antinodal pseudogap gets smaller with doping until it closes near $x\sim0.15$ (Fig. 7) [37]. In the momentum space, the low lying states near E_F form a 'Fermi arc' near the nodal region and spread gradually to the antinodal region with increasing doping (Fig. 5). The EDC at the nodal region shows a sharp peak, even for the $x=0.03$ sample, which increases in its spectral weight with doping (Fig. 7).

The measured Fermi surface seems to follow the band structure calculation [73]; this is consistent with the fact that both the hole-rich and hole-poor regions are made of the same underlying Cu–O states which resemble the intrinsic band structure. However, this should not be taken as a call to retreat back to band calculation. In some cases, the '*k*-spacing' Fermi surface mapping can be less informative than one would naively think. For example, an MDC-like k-space mapping actually cannot distinguish a Fermi liquid from Luttinger liquid; only a combination of MDC and EDC can [30]. The combined results of Figs. 5–7, both EDC and k-space mapping (basically MDC) make it clear that we have two electronic components and each has similar *k*-space dispersion. This, together with the lack of chemical potential shift [74], can be naturally explained by a nanoscale phase separation picture, such as stripes.

While the evidence for nanoscale phase separation in LSCO is very strong [66–70,75] and this is consistent with various neutron scattering evidence for stripes, the evidence for 1D electronic structure from photoemission is more subtle than envisioned in the early study [28], as the nodal states are also observed [31]. With the nanoscale phase separation picture in mind, we think that the two aspects of the low-lying electronic structure, the 2D-like Fermi surface and the straight segment near $(\pi, 0)$ region, are better explained in terms of the stripe picture (Fig. 8) [63,56,64,65]. In a phase-separation model for the stripe phase, Markiewicz [63] has shown that the dispersion of stripes can be interpreted essentially

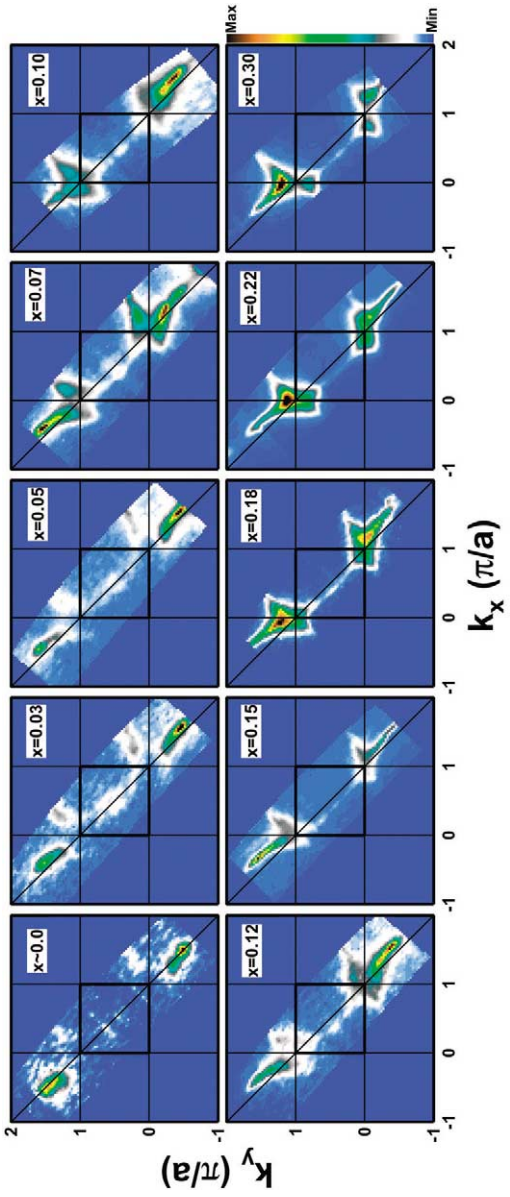

Fig. 5. Evolution of electronic structure with doping in $(La_{2-x}Sr_x)CuO_4$ ($x = 0$~0.30). The spectral weight is integrated within ±5 meV energy window near the Fermi level. The measurement geometry is the same as Fig. 4.

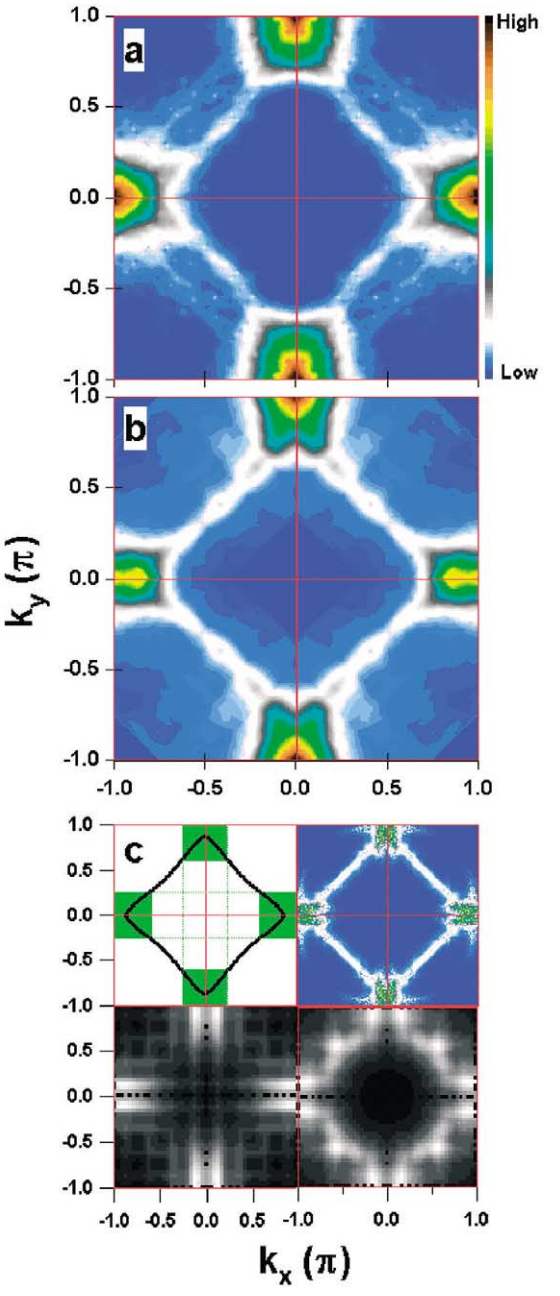

Fig. 8. Two aspects of the electronic structure in the stripe phase. (a) and (b) exemplify the measured low energy spectral weight of Nd-LSCO ($x = 0.15$) and LSCO ($x = 0.15$), respectively. The observed two features are schematically illustrated in (c) (upper-left panel): 2D-like Fermi surface (black line) and straight segments near (π, 0) and (0, π) regions. The spectral weight patterns calculated from stripe fluctuation (upper-right panel), from the site-centered stripe (lower-left panel) and bond-centered stripe (lower-right panel) are also included in (c).

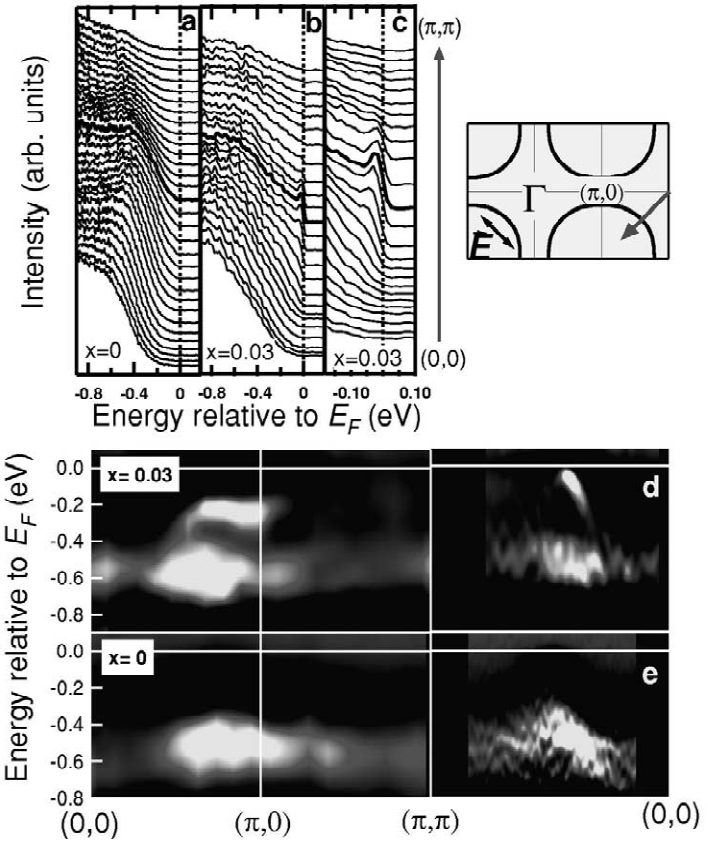

Fig. 6. ARPES spectra for LSCO with $x \sim 0$ and $x = 0.03$. Panels (a) and (b) are spectra along the (0, 0)–(π, π) nodal direction in the second Brillouin zone. Spectra for $x = 0.03$ are plotted on an enlarged scale in panel (c). Panels (d) and (e) represent energy dispersions deduced from the second derivative of the spectra. For LSCO with $x \sim 0$, the main feature is the lower Hubbard band (LHB) near 0.5 eV. Upon doping, new electronic states are created within the insulating gap while the position of the LHB shows little change.

as a superposition of the two end-phase dispersions, with superposed minigaps associated with the lattice periodicity. When considering stripe disordering and fluctuation, Salkola et al. [56] and Granath et al. [64] have shown how a system can exhibit what seems to be a Fermi surface of a two-dimensional metal although the dynamics of its low-energy electrons is entirely one-dimensional. The calculated spectral weight pattern based on stripe disorder/fluctuation (Fig. 8(c), upper-right panel) [56] is quite similar to those measured on Nd-LSCO and LSCO (Fig. 8(a) and (b)). Depending on the types of stripes, Zacher et al. [65] found that the site-centered stripes tend to generate low energy spectral weight near the antinodal region (Fig. 8(c), lower-left panel) while the bond-centered stripes create nodal spectral weight (Fig. 8(c), lower-right panel). A combination of these two may provide another way to understand the two aspects in the electronic structure.

While more work remains to be done to differentiate between various models, the phase separation and stripe formation have provided a most consistent picture for understanding the photoemission data of Nd-LSCO and LSCO as a whole, including coexistence of two components, pinning of chemical potential, the growth of near-E_F spectral weight, Z, with doping in the underdoped regime, and two aspects in the k-space distribution of the spectral weight. They are also in concert with all the other techniques which have provided independent evidence of phase separation and stripe formation in these systems.

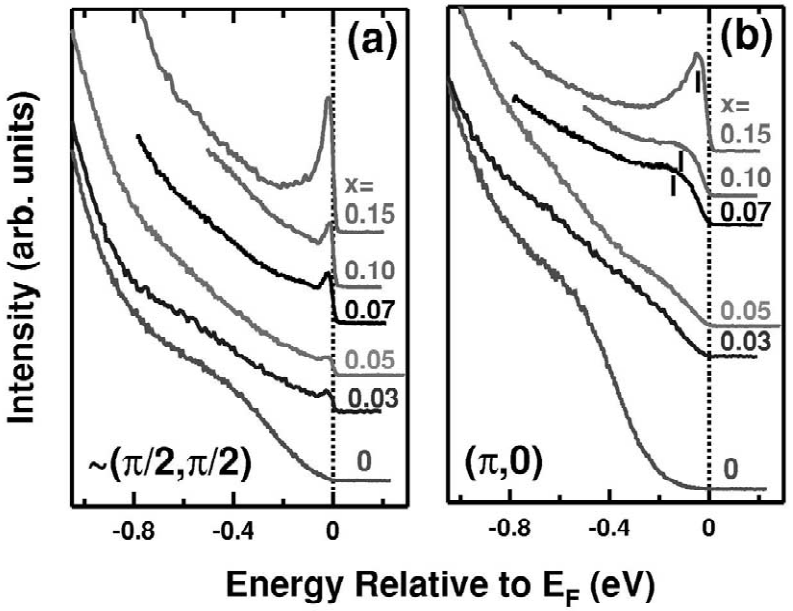

Fig. 7. ARPES spectra of LSCO at $k = k_F$ near the ~($\pi/2$, $\pi/2$) nodal region (a) and those at (π, 0) antinodal region (b), for various doping levels.

3. Bilayer splitting and Fermi surface topology of Bi2212

$Bi_2Sr_2CaCu_2O_8$ (Bi2212, $T_{c(max)} = 91$ K) is a model superconductor which has been most extensively studied by angle-resolved photoemission because it is easy to obtain a good surface by cleaving between its two consecutive BiO layers separated by weak Van der Waals bond. Many key insights about high temperature superconductivity have been drawn from ARPES study of this compound [20–22]. The determination of the Fermi surface is important because it underlies the physical properties of materials involved. It is also a basis on which the superconducting gap and pseudogap can be measured [21,22]. For many years, it was generally agreed that Bi2212 has a hole-like Fermi surface centered around Y(π, π), based on ARPES measurements using 22 eV photon energy. This hole-like Fermi surface picture was considered to be universal for Bi2212 with different doping levels [76,77]. The whole situation changed when an electron-like Fermi surface centered around Γ(0, 0) was proposed based on the measurement at 33 eV photon energy [78]. The main discrepancy boils down to whether the Fermi surface is closed or open near the M(π, 0) region. This M(π, 0) point, unfortunately, is highly complicated in Bi2212 because it is where the main bands, superstructure bands and shadows bands all cross the Fermi level. Some groups insisted on the single hole-like Fermi surface by dismissing the observation of an electron-like Fermi surface as a result of the interplay of matrix element effects with superstructure bands and shadow bands [79,80].

In light of the difficulty in making a definitive conclusion about the Fermi surface topology in Bi2212 because of the superstructure complication, we take a different approach by studying Pb-doped Bi2212 [33]. In this compound Pb replaces Bi in the BiO layers, disrupting the superstructure modulation and thus suppressing superstructure bands in Fermi surface determination. The measurements were carried out at various photon energies and under different polarizations in order to check the matrix element effect. In the absence of superstructure complications, the Fermi surface of Pb-Bi2212 actually consists of two sheets, as shown in Fig. 9(a). It turned out that the data show striking resemblance to theoretical simulations (Fig. 9(b)) for the same photon energy and polarization where the elusive

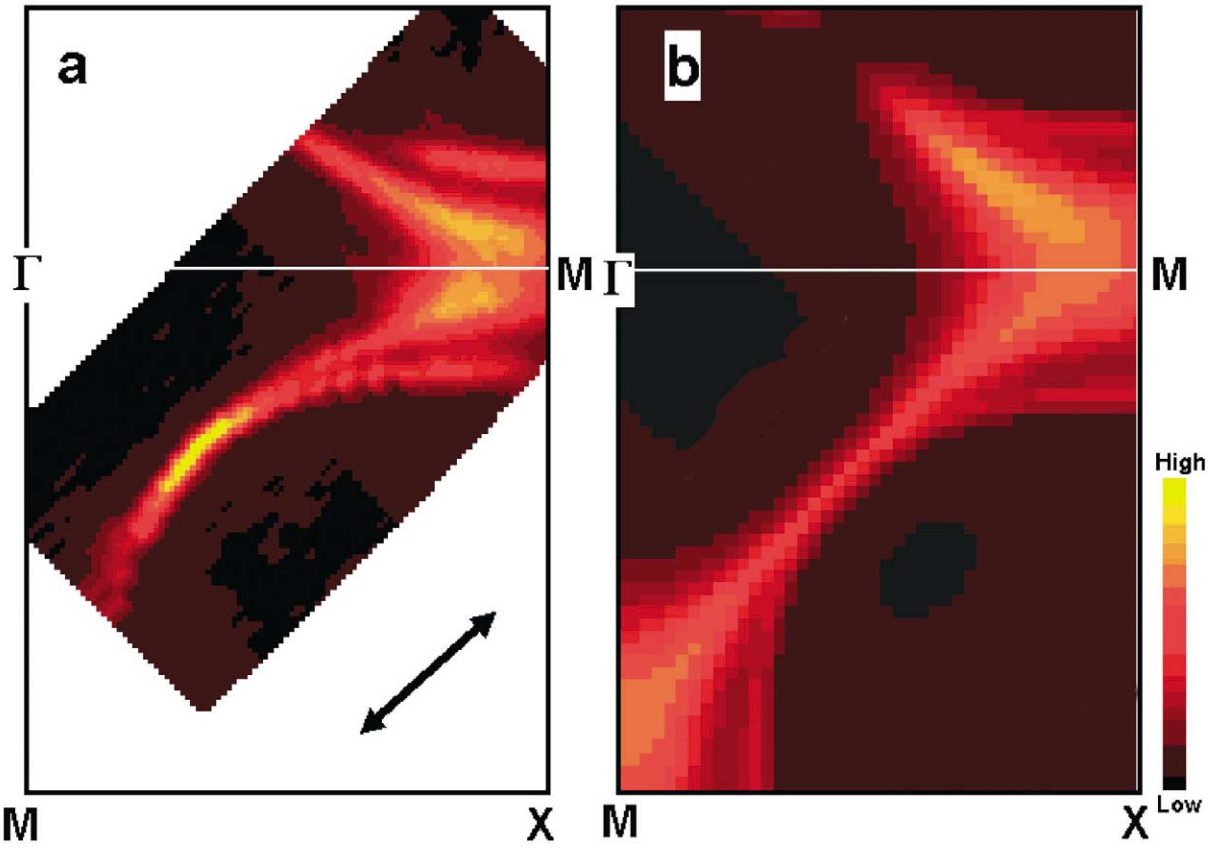

Fig. 9. Bilayer splitting in Pb-doped Bi2212. (a) shows the low energy spectral weight collected using 22 eV photon energy. The black arrow denotes the light polarization. (b) shows calculated ARPES intensity by Bansil et al. [81] for the same experimental condition. The two Fermi surface sheets come from the interaction of two adjacent CuO_2 planes in a unit cell of Bi2212.

bilayer splitting is considered [81]. Since there are two adjacent CuO_2 planes in a unit cell in Bi2212, the interaction between them gives rise to a bonding and an antibonding band, which further lead to two Fermi surface sheets [82]. For a long time this splitting was not identified and was stressed to result from novel physics [76]. The outer Fermi surface sheet, originating from the bonding band, is clearly a hole-like piece. The inner sheet, from the antibonding band, is very close to the M(π, 0) point, making it hard to tell whether it is electron-like or hole-like. Similar observations of two Fermi surface sheets have also been reported in Bi2212 recently [83,84]. The two Fermi surface sheets turned out to have very different photon energy dependence [33]. As an example, Fig. 10 shows the data taken at 55 eV photon energy, under the same geometry as that of Fig. 9(a). Only one Fermi surface sheet shows up and it is electron-like. Comparing this pattern with Fig. 9 suggests that only the inner piece of the Fermi surface is picked up at this photon energy.

The observation of two Fermi surface sheets and their different dependence on photon energy and polarization provide a unified picture of Fermi surface topology in Bi2212 and resolve the earlier controversy [78–80]. This explains why the Fermi surface in Bi2212 may show up as either hole-like or electron-like depending on which one is picked up at a given photon energy and polarization. It clearly indicates that the accepted picture of a single hole-like Fermi surface in Bi2212 is incorrect. This observation of the bilayer splitting, together with the complication already from the superstructure, asks for extra precaution to be exercised in analyzing data

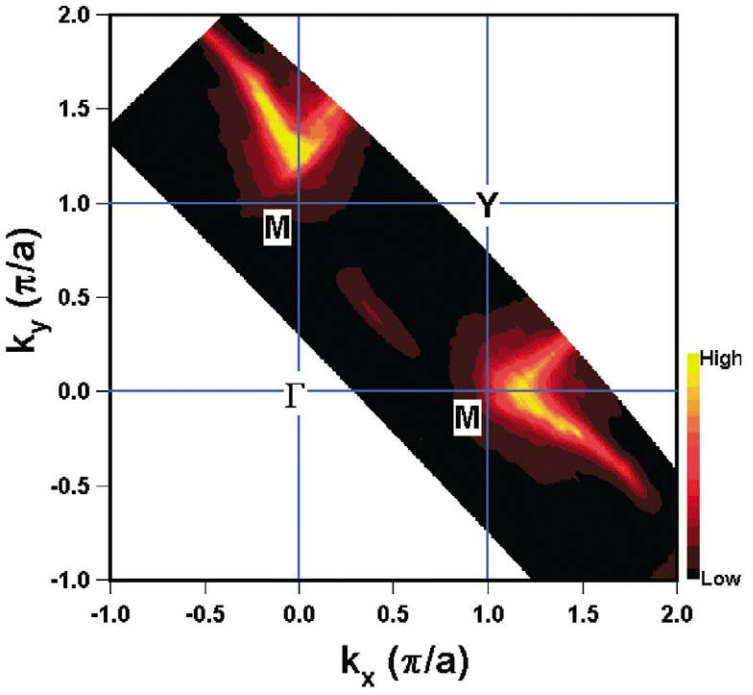

Fig. 10. Electron-like Fermi surface in Pb-doped Bi2212. The pattern shows low energy spectral weight at the Fermi level collected using 55 eV photon energy.

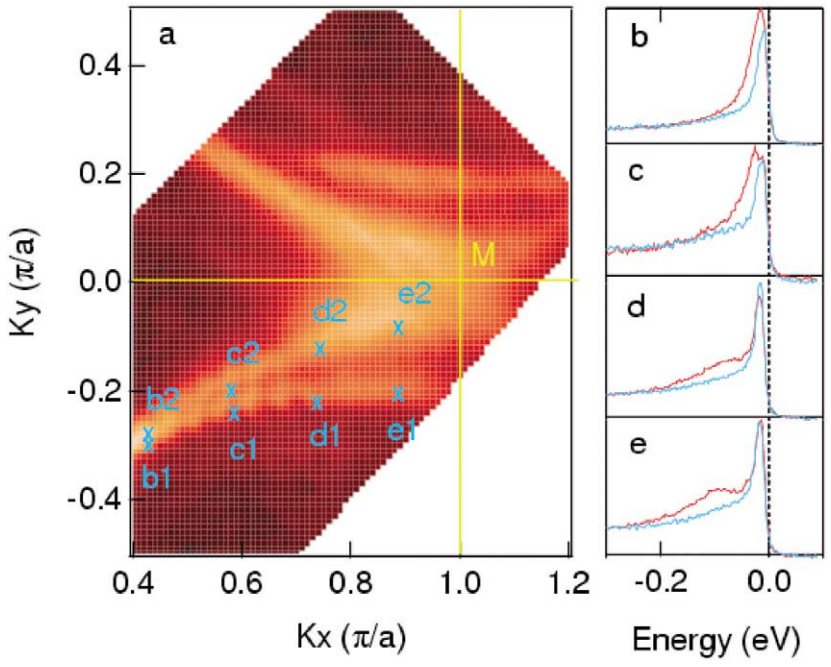

Fig. 11. (a) Spectral intensity at the Fermi level of Pb-Bi2212 ($T_c = 70$ K) measured at 20 K, and (b) EDCs on various Fermi surface locations for both bonding (blue lines from points b1, c1, d1, and e1) and antibonding (red lines from points b2, c2, d2, and e2) sheets.

in Bi2212, particularly when a quantitative analysis is attempted near the (π, 0) region without clear resolving of the bilayer splitting.

It was noticed that the EDC width near the (π, 0) antinodal region is usually broader than that near the nodal region, particularly for the underdoped samples [85,86]. The anisotropy is generally attributed to the spin scattering at $Q=(\pi, \pi)$, which connects the (π, 0) and (0, π) points in the moment space [85,86]. Such magnetic fluctuation is also considered as a possible pairing mechanism for high-T_c superconductivity [10]. While the broadening of the (π, 0) spectra in underdoped regime is a real effect as seen in single-layer compounds, such as $(La_{2-x}Sr_x)CuO_4$ and $(Ca_{2-x}Na_x)CuO_2Cl_2$, the quantitative analysis of (π, 0) data from Bi2212 is hindered by the bilayer splitting. The clear resolving of bilayer splitting in Bi2212 provides a good opportunity to address the issue of the anisotropy of electron scattering in high temperature superconductors, especially for overdoped cases where the resolving of bilayer Fermi surface is unambiguous. Fig. 11 shows EDCs along the Fermi surface on both bonding and antibonding sheets [36]. The EDC width is found to be nearly a constant at different Fermi surface locations; this is the case for both Fermi surface sheets, and for temperatures both above and below T_c [36]. This suggests that the effect of $Q=(\pi, \pi)$ scattering on quasiparticle dynamics is already negligible in the overdoped Bi2212 with T_c still as high as 70 K.

4. Strong electron–phonon coupling and strong electron–electron interaction in high temperature superconductors

It is generally believed that the unconventional normal state properties hold a key to understanding the microscopic origin of high temperature superconductivity. Because of its proximity to the Mott insulating state, strong electron–electron correlation has been emphasized to be held responsible [87]. This approach has an attractive feature in that the *d*-wave pairing is a natural consequence [10,11]. An alternative approach is to focus on modifying electron–phonon coupling theory [88,89], which has the advantage to naturally couple to the strong lattice effects observed [90,91]. So far there is no consensus on which of the two approaches is more proper to take despite the fact that the former approach has attracted much more attention than the latter. The earlier analysis of data from the high critical temperature (T_c), transport measurement, *d*-wave symmetry of the superconducting gap, and the isotope effect led to a conception that the electron–phonon coupling is rather weak and is not responsible for high temperature superconductivity [92]. Recent advancement of ARPES technique has made it possible to measure directly the electron self-energy, providing a good opportunity in addressing the issue, as electron–phonon coupling will result in effects in the electron self-energy.

Using the angular mode of the Scienta analyzer, the original data measured are a two-dimensional image which represents the photoelectron intensity as a function of angle (and then momentum) and energy, as exemplified in Fig. 12(a) for LSCO. The measurement has provided a novel way of analyzing the data. In contrast to the traditional energy distribution curves (EDC, intensity as a function of energy for a given momentum) (Fig. 12(c)) which are usually complicated with background and Fermi function cutoff, the momentum distribution curves (MDC, intensity as a function of momentum for a given energy) (Fig. 12(b)) show a well-defined peak with a flat background; they can be further fitted with a Lorentzian lineshape [93]. The effectiveness of momentum space scanning at fixed energy for cuprate study was shown by Aebi et al. [94] in their earlier mapping of the Fermi surface. As seen from Eq. (1), since the band dispersion ϵ_k can be approximated as $\epsilon_k = v_0 k$ in the vicinity of the Fermi level, and assuming weak momentum dependence of self-energy $\Sigma(k, \omega)$, $A(k, \omega)$ indeed exhibits a Lorentzian lineshape as a function of momentum k for a given binding energy $\hbar\omega$. By fitting a series of MDCs at different binding energies to obtain MDC position $\tilde{k}$ and width (Γ, full-width at half maximum, FWHM), one can directly extract electron self-energy $\Sigma = \mathrm{Re}\Sigma + i\mathrm{Im}\Sigma$ as: $\mathrm{Re}\Sigma = \hbar\omega - \tilde{k}v_0$ and $\mathrm{Im}\Sigma = (\Gamma/2)v_0$.

We have applied this method to various high temperature superconductors, including Bi2212, Bi2201 ($Bi_2Sr_2CuO_6$) and LSCO systems [29,32,35,38]. The dispersion along the nodal direction and the MDC width for $(La_{2-x}Sr_x)CuO_4$ are

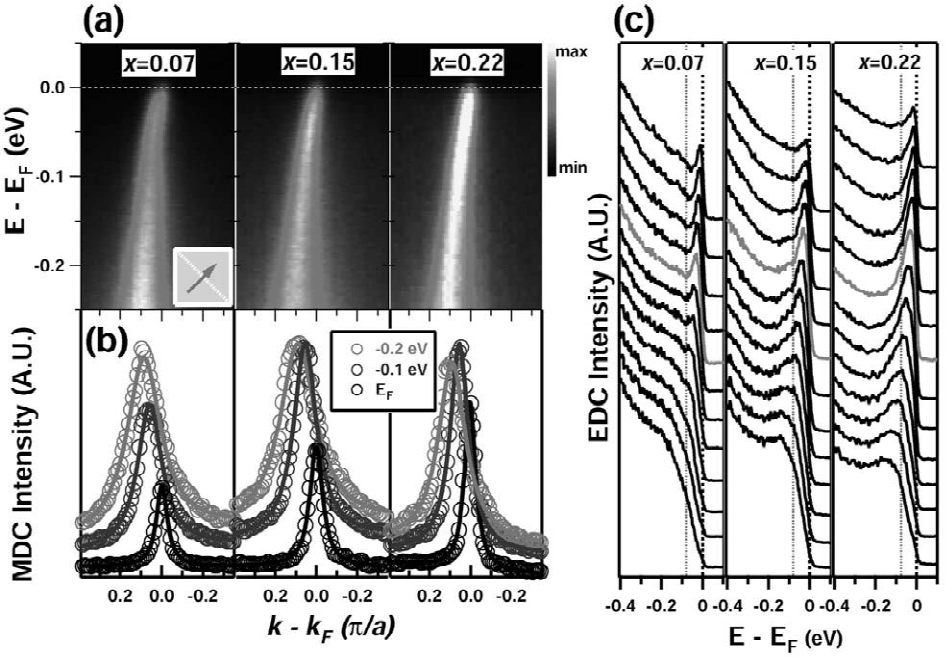

Fig. 12. Original data of LSCO samples with different dopings and the corresponding EDCs and MDCs. (a) shows the original data taken on LSCO samples with $x=0.07$, 0.15 and 0.22 along the nodal direction. The corresponding MDCs at different binding energies (0, 0.10 and 0.20 eV) are shown in (b). The open circles in (b) represent measured MDCs while the solid lines are Lorentzian fit. (c) shows EDCs for these three samples. A double-peak feature can be seen in some EDCs, which is particularly clear for $x=0.07$, giving rise to a peak–dip–hump structure. The vertical dashed lines represent the dip position around 80 meV.

shown in Fig. 13 where the doping x covers the whole range [38]. As seen from Fig. 13(a), the high binding energy part of the dispersion follows a straight line, and a deviation from the line ('kink') occurs at lower binding energy near ~80 meV. The kink effect is present throughout the entire doping levels at a similar energy scale. In the meantime, there is an accelerated drop on the MDC width curves (Fig. 13(b)) at a similar energy where the kink occurs in dispersion, particularly obvious for low doping levels. This nodal kink effect is universal in high T_c materials as it is seen in LSCO, Bi2212 and Bi2201 with various dopings (Fig. 14) [32]; it is also seen at different temperatures, both above T_c and below T_c (Fig. 14) [32,38]. The kink effect clearly indicates an energy scale and signals a coupling of quasiparticles with some low energy excitations [29]. If one believes the kink effect seen for different superconductors, at entire doping range, and at different temperatures, is from the same origin, the only known scenario left is the coupling of quasiparticles with phonons [32,38]. The absence of magnetic mode in LSCO and the observation of a kink both below T_c and above T_c all speak against the magnetic mode as the origin of the kink effect along the nodal direction, as proposed by some groups for Bi2212 [95,96]. Recently, a lower energy kink has been identified near the (π, 0) antinodal region in Bi2212 [97]. This antinodal kink is a distinct effect as it is seen only below T_c and has a different doping dependence in its energy which is also generally lower than that of the nodal kink [97].

There are a number of experimental fingerprints that can be used to further check on the nature of the low energy excitation involved, such as the EDC lineshape, dispersion and MDC width. The key issue is the existence of an energy scale. For the conventional Fermi liquid theory, and the Marginal Fermi Liquid (MFL) theory as proposed to account for the anomalous normal state properties of optimally doped high temperature superconductors [13], the EDCs show only one peak. On the other hand, for

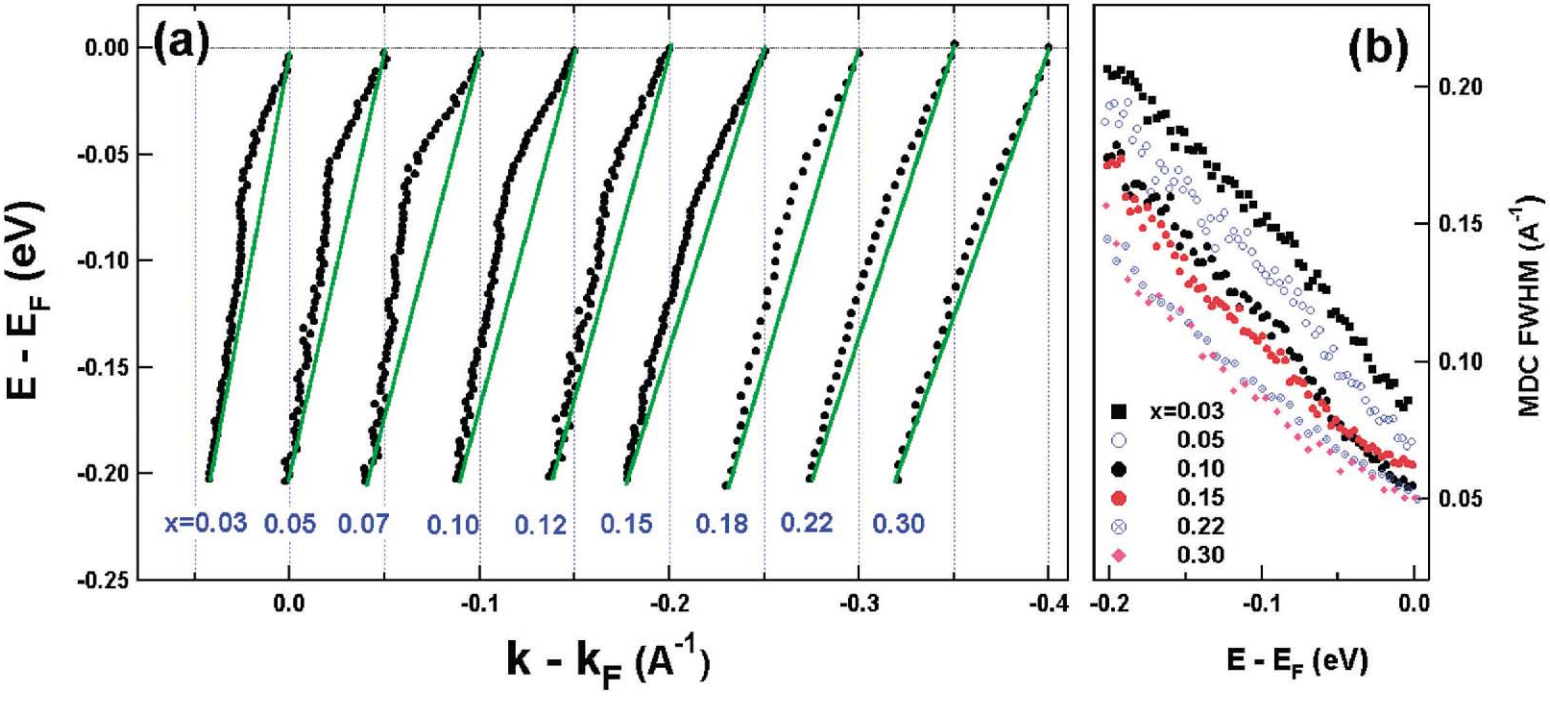

Fig. 13. Dispersion (a) and MDC width (FWHM)(b) of LSCO samples ($x = 0.03 \sim 0.30$) measured along the nodal direction, as determined from fitting MDCs. For clarity, the dispersion in (a) is offset horizontally along the momentum axis. The green lines in (a) connect the points in dispersion at E_F and 0.2 eV which approximately represents the bare band; they also serve as guides to the eye to identify the kink in dispersion. The MDC width (b) shows an overall decrease with increasing doping. A slight drop in MDC width is discernible at a binding energy of ~80 meV, particularly obvious for lower doping samples.

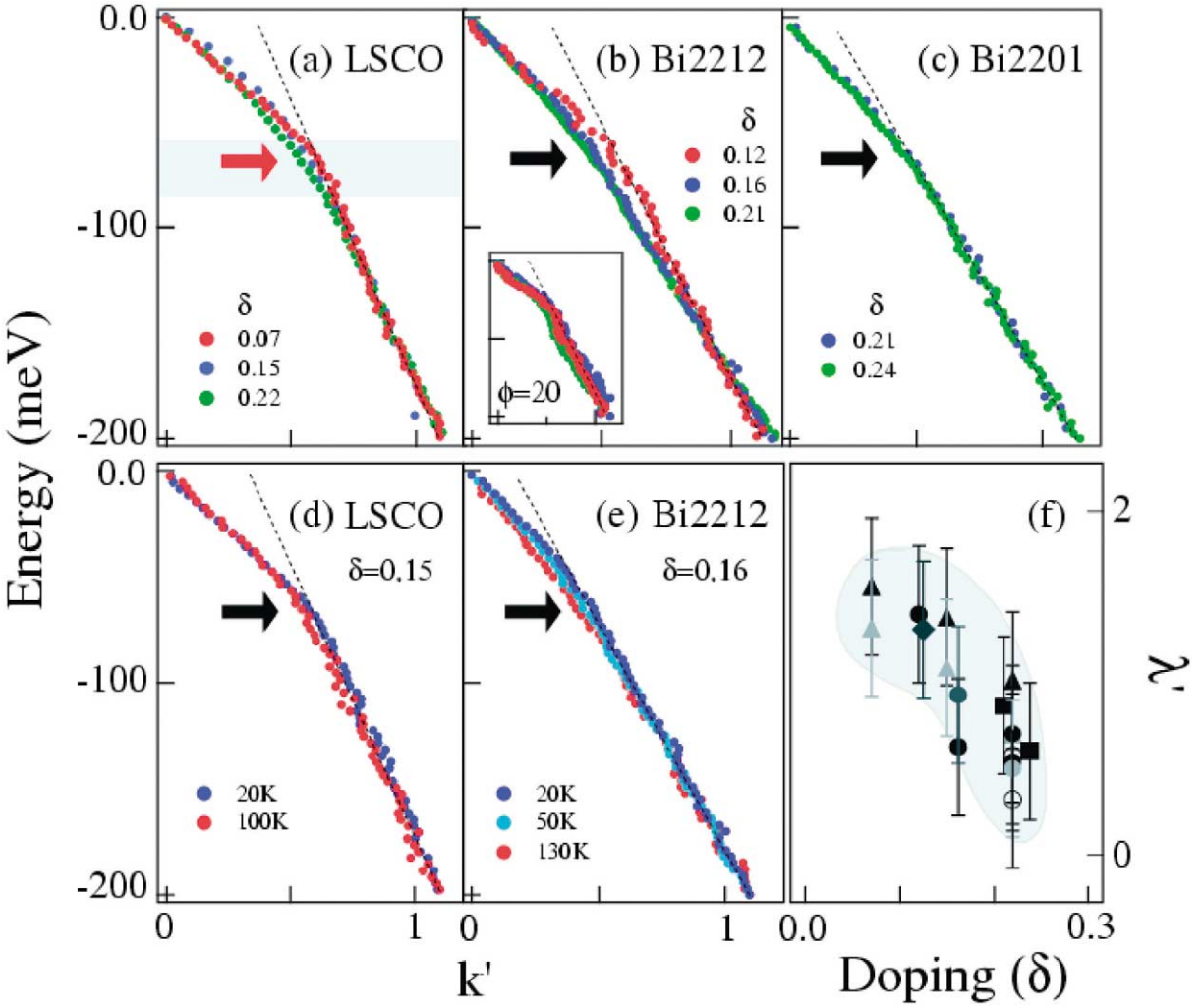

Fig. 14. Ubiquitous observation of kink in various high temperature superconductors. Top panels (a, b and c) show dispersion along the nodal direction for LSCO, Bi2212 and Bi2201 at different dopings. The arrows indicates the kink position in dispersions and the dotted lines are guides to the eye. (d) and (e) show temperature dependence of the kink effect in LSCO and Bi2212, respectively. The doping dependence of the effective coupling constant is shown in (f).

electron–phonon coupling system, the EDCs show two peaks, one broad peak at high binding energy and one sharp peak near the Fermi level, the position of the dip between them representing the energy scale of the phonon involved. Such a peak–dip–hump structure can be seen from the simulated EDCs (Fig. 15(e)) and has been observed in some canonical electron–phonon coupling systems, such as the Be(0001) surface state (Fig. 15(d)) [98,99]. Similar observation of the double peak features in the nodal direction in Bi2212 (Fig. 15) [32], LSCO (Fig. 12(c)) [38] and Bi2201 [39] provides a qualitative but compelling evidence in favor of the electron–phonon coupling. Here we note that the ARPES setup at the ALS has advantages to address the issue because of: (A) its superior flux which results in better signal to noise ratio; (B) its variable photon energy well beyond that of the normal incident monochromators (NIM) typically used for studying cuprates; and (C) its variable polarization, so that a proper configuration can be found so that the 'peak–dip–hump' structure is perfectly well seen beyond the EDC

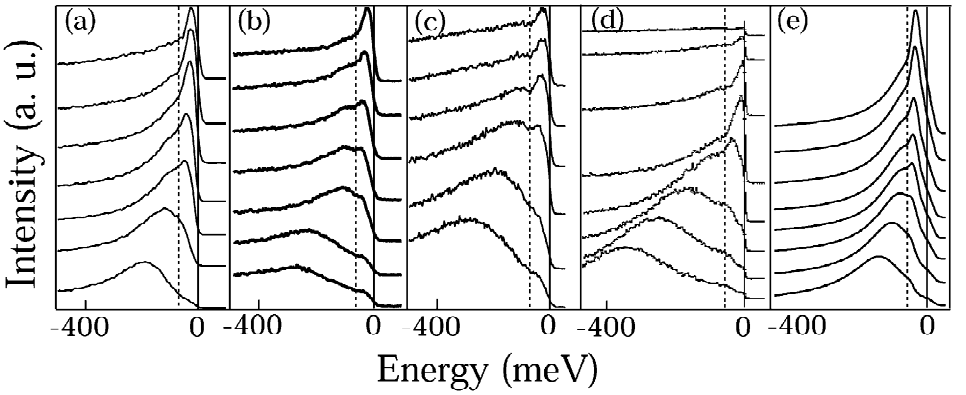

Fig. 15. Double-peak features in the photoemission spectra due to electron–phonon coupling. (a), (b) and (c) show raw EDCs measured along the nodal direction for overdoped Pb-Bi2212 ($T_c = 70$ K), for optimally doped Bi2212 ($T_c = 91$ K) and for underdoped Bi2212 ($T_c = 84$ K), respectively. Raw EDCs for Be(0001) surface are shown in (d) and simulated EDCs are shown in (e). The dashed lines represent the approximate 'dip' position which is related to the known phonon energy.

background. An example is that we can see the peak–dip–hump structure in Bi2201 much better than using NIM. Its observation in Bi2201 is important in this case because T_c is low so that we can investigate the intrinsic lineshape at low temperature without the interference of superconductivity.

The dispersion and MDC width can be quantitatively understood in terms of electron–phonon (el–ph) coupling, together with electron–electron (el–el) interaction and electron scattering from impurities (el–im) [38]. These are the three major contributions to the electron self-energy in a real system [98–100]. For the dispersion (Fig. 13(a)), the deviation from the linear bare dispersion reflects the contribution solely from the el–ph coupling; the el–el part is linear and is buried in the bare dispersion and the scattering from impurity does not contribute. The dispersion in the entire doping range can be well fitted in terms of an el–ph coupling scheme, as shown in Fig. 16(a). We note that the obtained Debye frequency ω_D represents only a phonon frequency cutoff; there are a number of low energy phonons present in cuprates which can be involved in electron–phonon coupling.

The measured MDC width can be decomposed into three contributions, as seen from Fig. 16(b) where the el–el contribution to the imaginary part of self-energy is approximated as $\mathrm{Im}\Sigma'_{\mathrm{el-el}} = \beta\omega^2$. The obtained β value ($2 \sim 3$ eV^{-1}) is significantly larger than that (~ 0.1 eV^{-1}) observed in Mo [100] and Be [98], signifying the presence and importance of el–el correlation in cuprate superconductors. We also note that, since various effects all contribute to the MDC width, it may not be as sensitive as the dispersion in showing the drop of scattering rate due to el–ph coupling. However, a drop is still clearly discernible in Fig. 16 (and Fig. 13(b)), particularly for less doped samples. The observation of the drop results from improved signal to noise ratio; we have seen this even more clearly in Bi2201 and Bi2212 with 55 eV photon energy. This is in concert with the observations of the peak–dip–hump structure in EDC and kink in the MDC dispersion because these are all closely related.

Therefore, by measuring the electron self-energy directly from ARPES, we have found evidence of strong electron–phonon coupling and electron–electron interaction in high temperature superconductors. Combining them together helps understand many unusual physical properties. Since the electron–phonon coupling strongly influences the low energy electron dynamics, it must be included seriously in any microscopic theory of superconductivity, in addition to electron–electron interaction.

Acknowledgements

We thank P. Bogdanov, A. Lanzara, S.A. Kellar, E.D. Lu, W.L. Yang, T. Yoshida, A. Fujimori, T. Noda, T. Kakishita, H. Eisaki and S. Uchida for their collaborations in experiments and discussions. The experiment, performed at the ALS of LBNL, is

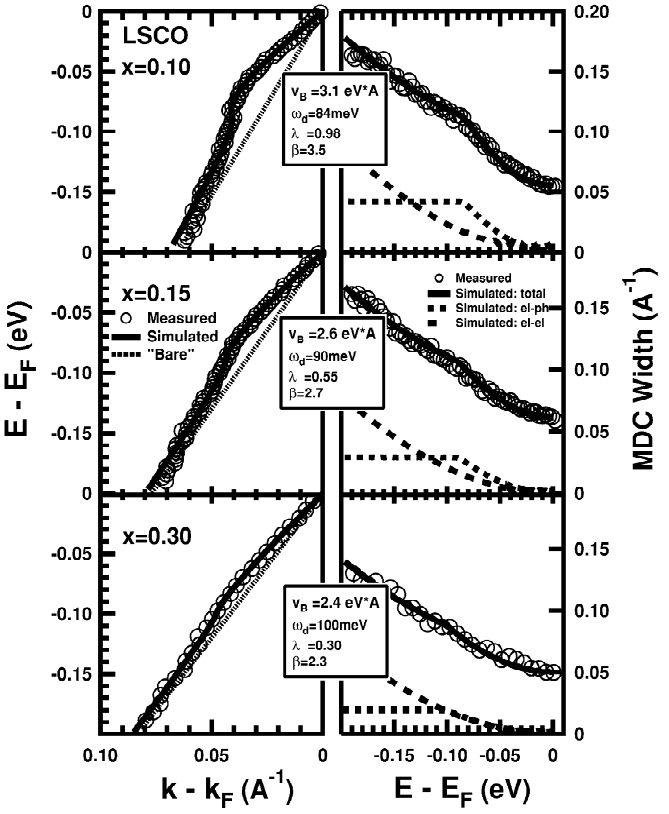

Fig. 16. Simulation of the dispersion (left panels) and MDC width (right panels) for LSCO with three typical dopings. The simulation includes self-energy contributions from el–ph coupling, el–el interaction and impurity scattering. In (a) the measured dispersion (open circles) is fitted with a standard el–ph approach: the fitted dispersion is represented as solid lines and the fitted bare dispersion is shown as dashed lines. The fitted parameters are included in the textbox on each panel. In (b) the measured MDC width (open circles) is decomposed into three components: (1) The offset at E_F is from the impurity scattering and is taken as a constant over the whole energy range; (2) The el–ph coupling part is obtained from the same parameters of dispersion fitting; (3) The el–el contribution is approximated by taking $\mathrm{Im}\Sigma''_{\mathrm{el-el}} = \beta\omega^2$ with β being a free parameter so that the overall fitted MDC width (solid lines) best matches the measured one. The β value used is also included in the textbox and the corresponding el–el contribution is plotted as blue dashed lines.

supported by the Department of Energy's Office of Basics Science Division, Division of Materials Science. This Division also supported this research through the Stanford Synchrotron Radiation Laboratory.

References

[1] J.G. Bednorz, K.A. Muller, Zeitschrift fur Physik B 64 (1986) 189.
[2] See, e.g., reviews in the special issue on correlated electron systems, Science 288 (2000) 461–482.
[3] Y. Tokura, T. Arima, Jap. J. Appl. Phys., Part 1 29 (1990) 2388.
[4] R.J. Cava, J. Am. Ceram. Soc. 83 (2000) 5.
[5] B. Batlogg et al., Physica C 235–240 (1994) 130; B. Batlogg, C. Varma, Phys. World 13 (2000) 33.
[6] C.E. Gough et al., Nature 326 (1987) 855.
[7] J. Bardeen, L.N. Cooper, J.R. Schrieffer, Phys. Rev. B 108 (1957) 1175.
[8] W.L. McMillan, J.M. Rowell, Phys. Rev. Lett. 14 (1965) 108.
[9] C.C. Tsuei, J.R. Kirtley, Rev. Mod. Phys. 72 (2000) 969, and references therein.
[10] D.J. Scalapino, Phys. Rep. 250 (1995) 329.
[11] D. Pines, P. Monthoux, J. Phys. Chem. Solid 56 (1995) 1651.
[12] D.J. Scalapino, Science 284 (1999) 1282; J. Orenstein, Nature 72 (1999) 333, and references therein.

[13] C.M. Varma, P.B. Littlewood, S. Schmitt-Rink, Phys. Rev. Lett. 63 (1989) 1996.
[14] For a review, see T. Timusk, B. Statt, Rep. Prog. Phys. 62 (1999) 61.
[15] S. Huefner, Photoelectron Spectroscopy: Principles and Applications, Springer, 1995.
[16] Z.-X. Shen, D.S. Dessau, Phys. Rep. 253 (1995) 1; Z.-X. Shen et al., Science 267 (1995) 343.
[17] Special Issue of Journal of Electron Spectroscopy and Related Phenomena, 117–118, 2001.
[18] L. Hedin, S. Lundqvist, in: F. Seitz, D. Turnbull, H. Ehrenreich (Eds.), Solid State Physics, Academic Press, 1969.
[19] M. Randeria et al., Phys. Rev. Lett. 74 (1995) 4951.
[20] C.O. Olsen et al., Science 245 (1989) 731.
[21] Z.-X. Shen et al., Phys. Rev. Lett. 70 (1993) 1553.
[22] D.S. Marshall et al., Phys. Rev. Lett. 76 (1996) 4841; A.G. Loeser et al., Science 273 (1996) 325; H. Ding et al., Nature 382 (1996) 51.
[23] N.P. Armitage et al., Phys. Rev. Lett. 86 (2001) 1126; T. Sato et al., Science 291 (2001) 1517.
[24] A. Chainani et al., Phys. Rev. Lett. 85 (2001) 1966.
[25] A. Damascelli et al., Phys. Rev. Lett. 85 (2000) 5194.
[26] Y.D. Chuang et al., Science 292 (2001) 1509.
[27] J.D. Denlinger et al., Cond-mat/0107429.
[28] X.J. Zhou et al., Science 286 (1999) 268.
[29] P.V. Bogdanov et al., Phys. Rev. Lett. 85 (2000) 2581.
[30] D. Orgad et al., Phys. Rev. Lett. 86 (2001) 5362.
[31] X.J. Zhou et al., Phys. Rev. Lett. 86 (2001) 5578.
[32] A. Lanzara et al., Nature 412 (2001) 510.
[33] P.V. Bogdanov et al., Phys. Rev. B 64 (2001) 180505.
[34] T. Yoshida et al., Phys. Rev. B 63 (2001) 220501.
[35] Z.-X. Shen, A. Lanzara, S. Ichihara, N. Nagaosa, cond-mat/0108381 (2001).
[36] P.V. Bogdanov et al., submitted to Phys. Rev. Lett.
[37] T. Yoshida et al., Cond-mat/0206469 (2002).
[38] X.J. Zhou et al., to be submitted.
[39] A. Lanzara et al., to be submitted.
[40] For a review, see V.J. Emery, S.A. Kivelson, J.M. Tranquada, Proc. Natl. Acad. Sci. USA 96 (1999) 8814; J. Zaanen, J. Phys. Chem. Solids 59 (1998) 1769, and references therein.
[41] S.A. Kivelson, V.J. Emery, in: K.S. Bedell et al. (Ed.), Strongly Correlated Electronic Materials: The Los Alamos Symposium, 1993, Addison-Wesley, Reading, MA, 1994, pp. 619–650.
[42] V.J. Emery, S.A. Kivelson, O. Zacher, Phys. Rev. B 56 (1997) 6120.
[43] J. Zaanen, O. Gunnarson, Phys. Rev. B 40 (1989) 7391.
[44] D. Poilbanc, T.M. Rice, Phys. Rev. B 39 (1989) 9749.
[45] H.J. Schulz, J. Phys. 50 (1989) 2833.
[46] C. Castellani, C.D. Castro, M. Grilli, Phys. Rev. Lett. 75 (1995) 4650.
[47] A.H. Castro Neto, D. Hone, Phys. Rev. Lett. 76 (1996) 2165.
[48] J. Zaanen, M.L. Horbach, W.V. Saaloos, Phys. Rev. B 53 (1996) 8671.
[49] H. Eskes et al., Phys. Rev. B 54 (1996) R724; H. Eskes et al., Phys. Rev. B 58 (1998) 6963.
[50] C.M. Smith et al., Phys. Rev. B 58 (1998) 453.
[51] S.A. Kivelson et al., Nature 393 (1998) 550.
[52] J. Zaanen, O.Y. Osman, W. Van Saaloos, Phys. Rev. B 58 (1998) R11868.
[53] N. Hasselmann et al., Phys. Rev. Lett. 82 (1999) 2135.
[54] J. Zaanen, A.M. Oles, Ann. Phys. 5 (1996) 224.
[55] C. Nayak, F. Wilczek, Phys. Rev. Lett. 78 (1997) 2465.
[56] M.I. Salkola, V.J. Emery, S.A. Kivelson, Phys. Rev. Lett. 77 (1996) 155.
[57] S.R. White, D.J. Scalapino, Phys. Rev. Lett. 81 (1998) 3227.
[58] S.R. White, D.J. Scalapino, Phys. Rev. Lett. 80 (1998) 1272.
[59] J. Zaanen, M.L. Horbach, W.V. Saaloos, Phys. Rev. B 53 (1996) 8671.
[60] T. Tohyama et al., Phys. Rev. Lett. 82 (1999) 4910.
[61] A.V. Balatsky, P. Bourges, Phys. Rev. Lett. 82 (1999) 5337.
[62] M. Fleck et al., Phys. Rev. Lett. 84 (2000) 4962.
[63] R.S. Markiewicz, Phys. Rev. B 62 (2000) 1252.
[64] M. Granath et al., Phys. Rev. B 65 (2002) 184501.
[65] M.G. Zacher et al., Phys. Rev. Lett. 85 (2000) 2585; M.G. Zacher et al., Phys. Rev. B 65 (2002) 45109.
[66] J.M. Tranquada et al., Nature 375 (1995) 561; J.M. Tranquada et al., Phys. Rev. B 59 (1999) 14712.
[67] M.v. Zimmermann et al., Europhys. Lett. 41 (1998) 629.
[68] A.W. Hunt et al., Phys. Rev. Lett. 82 (1999) 4300.
[69] T. Noda, H. Eisaki, S. Uchida, Science 286 (1999) 265.
[70] K. Yamada et al., Phys. Rev. B 57 (1998) 6165.
[71] H.A. Mook et al., Nature 395 (1998) 580; H.A. Mook et al., Nature 401 (1999) 145.
[72] A. Ino et al., Phys. Rev. B. 62 (2000) 4137.
[73] J.-H. Xu et al., Phys. Lett. A 120 (1987) 489; W.E. Pickett, Rev. Mod. Phys. 61 (1989) 433.
[74] A. Ino et al., Phys. Rev. Lett. 79 (1997) 2101.
[75] M. Matsuda et al., Phys. Rev. B 62 (2000) 9148; M. Matsuda et al., Phys. Rev. B 65 (2002) 134515.
[76] H. Ding et al., Phys. Rev. Lett. 76 (1996) 1533.
[77] H. Ding et al., Phys. Rev. Lett. 78 (1997) 2628.
[78] Y.D. Chuang et al., Phys. Rev. Lett. 83 (1999) 3717.
[79] H.M. Fretwell et al., Phys. Rev. Lett. 84 (2000) 4449.
[80] S.V. Borisenko et al., Phys. Rev. Lett. 84 (2000) 4453.
[81] A. Bansil, M. Lindroos, Phys. Rev. Lett. 83 (1999) 5154.
[82] S. Massida, J. Yu, A.J. Freeman, Physica C 152 (1988) 251; H. Krakauer, W.E. Pickett, Phys. Rev. Lett. 60 (1998) 1665; M.S. Hybertsen, L.F. Mattheiss, Phys. Rev. Lett. 60 (1988) 1661.
[83] D.L. Feng et al., Phys. Rev. Lett. 86 (2001) 5550.
[84] Y.D. Chuang et al., Phys. Rev. Lett. 87 (2001) 117002.
[85] J.C. Campuzano et al., Phys. Rev. Lett. 83 (1999) 3709.
[86] Z.-X. Shen, J.R. Schrieffer, Phys. Rev. Lett. 78 (1997) 1771.
[87] P.W. Anderson, The Theory of Superconductivity in the High-T_c Cuprates, Princeton University Press, Princeton, NJ, 1997.
[88] K.A. Muller, Physics C 341–348 (2000) 11.
[89] For a review, see M.L. Kulic, Physics Reports 338 (2000) 1.
[90] R.J. McQueeney et al., Phys. Rev. Lett. 87 (2001) 77001, and references therein.
[91] J. Hofer et al., Phys. Rev. Lett. 84 (2000) 4192.
[92] P.B. Allen, Nature 412 (2001) 494.

[93] T. Valla et al., Science 285 (1999) 2110.
[94] P. Aebi et al., Phys. Rev. Lett. 72 (1994) 2757.
[95] A. Kaminski et al., Phys. Rev. Lett. 85 (2000) 2581; M.R. Norman et al., Phys. Rev. Lett. 79 (1997) 3506.
[96] P.D. Johnson et al., Phys. Rev. Lett. 87 (2001) 177007.
[97] A.D. Gromko et al., Cond-mat/0202329 (2002).
[98] M. Hengsberger et al., Phys. Rev. B 60 (1999) 10796.
[99] T. Balasubramanian et al., Phys. Rev. B 57 (1998) R6866; S. Lashell et al., Phys. Rev. B 61 (2000) 2371.
[100] T. Valla et al., Phys. Rev. Lett. 83 (1999) 2085.